Lawrence Berkeley National Laboratory

Title

Enhanced phase contrast transfer using ptychography combined with a pre-specimen phase plate in a scanning transmission electron microscope

Permalink

Authors

Yang, Hao
Ercius, Peter
Nellist, Peter D
et al.

Publication Date

DOI

Peer reviewed
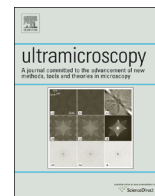
Enhanced phase contrast transfer using ptychography combined with a pre-specimen phase plate in a scanning transmission electron microscope

Hao Yang [a], Peter Ercius [a], Peter D. Nellist [b], Colin Ophus [a],*

[a] Molecular Foundry, Lawrence Berkeley National Laboratory, Berkeley, CA 94720, USA
[b] Department of Materials, University of Oxford, Parks Road, Oxford OX1 3PH, UK

ABSTRACT

The ability to image light elements in both crystalline and noncrystalline materials at near atomic resolution with an enhanced contrast is highly advantageous to understand the structure and properties of a wide range of beam sensitive materials including biological specimens and molecular hetero-structures. This requires the imaging system to have an efficient phase contrast transfer at both low and high spatial frequencies. In this work we introduce a new phase contrast imaging method in a scanning transmission electron microscope (STEM) using a pre-specimen phase plate in the probe forming aperture, combined with a fast pixelated detector to record diffraction patterns at every probe position, and phase reconstruction using ptychography. The phase plate significantly enhances the contrast transfer of low spatial frequency information, and ptychography maximizes the extraction of the phase information at all spatial frequencies. In addition, the STEM probe with the presence of the phase plate retains its atomic resolution, allowing simultaneous incoherent Z-contrast imaging to be obtained along with the ptychographic phase image. An experimental image of Au nanoparticles on a carbon support shows high contrast for both materials. Multislice image simulations of a DNA molecule shows the capability of imaging soft matter at low dose conditions, which implies potential applications of low dose imaging of a wide range of beam sensitive materials.

Published by Elsevier B.V.

1. Introduction

Imaging light elements such as biological specimens and molecular hetero-structures at atomic resolution has remained challenging due to the fact that high-energy electrons are weakly scattered by the sample, leading to only a small phase shift of the incident electron wave. For imaging such weakly scattering materials, coherent phase imaging provides a higher image contrast than incoherent amplitude contrast from thermal diffuse scattering and spectroscopic signals [1]. Phase contrast imaging is generally performed in the conventional transmission electron microscope (CTEM) using deliberately injected lens aberrations. Although CTEM is widely used in low dose imaging of weakly scattering biological structures, its contrast transfer function is not efficient especially at low spatial frequencies [2]. To gain the necessary contrast, a large defocus has to be used which produces a nonlinear effect on the image contrast [3]. This effect becomes more pronounced in high resolution TEM (HRTEM) and often

requires careful comparison with image simulations for structure interpretation. The introduction of a post-specimen phase plate in TEM enhances the low spatial frequency contrast transfer [4,5], and there continues to be considerable interests in the development of such physical phase plates.

STEM on the other hand is best known for its incoherent "Z-contrast" imaging using an annular dark field detector (ADF) and simultaneous spectroscopy capabilities. However these incoherent imaging modes are unable to match the dose efficiency of coherent phase contrast for imaging weak phase objects. Coherent bright field (BF-) STEM utilises only a small portion of the coherent scattering signal and thus gives a poor efficiency, and developing an efficient phase contrast imaging method in STEM is highly desirable. It has been shown possible to improve the efficiency of phase contrast through detector geometry innovations, for example using an annular detector to form the annular bright field (ABF) imaging [6,7] and a segmented detector for differential phase contrast (DPC) imaging [8–10].

Recent developments in high speed cameras enables the acquisition of two dimensional diffraction patterns at every probe position of a two dimensional electron beam raster across the specimen, forming an information-rich four dimensional STEM

* Corresponding author.
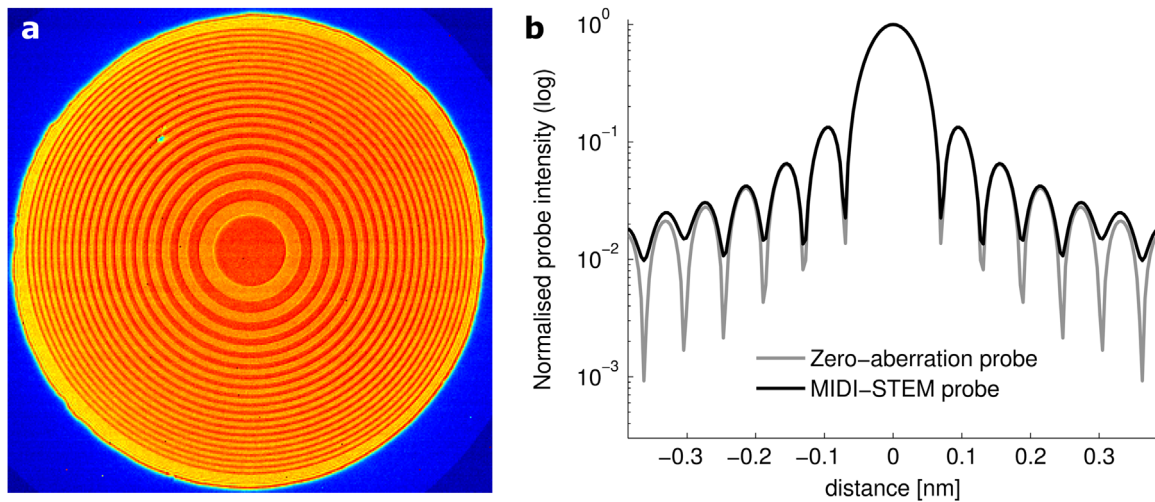 E-mail address: clophus@lbl.gov (C. Ophus).

Fig. 1. (a) An averaged convergent beam electron diffraction (CBED) pattern formed by scanning a MIDI-STEM electron probe over an ultra-thin amorphous carbon sample. The MIDI-STEM probe is formed using a pre-specimen *Fresnel* phase plate with a 20-ring pairs geometry located at the condenser aperture plane. Colormap heat is used. (b) Comparison of real space electron probe intensity (log-scale) under zero lens aberrations with and without the phase plate, showing that the real space MIDI-STEM probe has an atomically sharp central peak similar to that of the zero lens aberrations probe, but with enhanced probe tails.

(4D-STEM) dataset. Various methods have been demonstrated which allow phase information to be extracted using virtual detector geometries through post-acquisition processing. The atomic electric field within a thin specimen can be mapped out [11] using a "first moment" [12] DPC detector. Ptychography has been shown as an efficient phase retrieval method that makes an efficient use of the information redundancy in the 4D-data [13], allowing the formation of an efficient phase contrast under zero lens aberrations to be combined with simultaneously recorded incoherent Z-contrast imaging. Ptychography gives an improved phase contrast transfer and better image signal to noise ratio (SNR) compared to existing phase contrast images including DPC and ABF [14]. Ptychography is a technique first developed by Hoppe [15] to retrieve the object phase using diffraction patterns acquired from a sequential array of overlapping illuminated areas. Ptychography has been demonstrated at both electron [16,17] and X-ray [18,19] wavelengths to enhance the image contrast and resolution [20]. Due to limited camera speed, a widely adopted electron ptychography approach is to use highly defocused probes that illuminate a wide region of the sample to provide a large field of view while still limiting the number of probe positions [21–23]. Such defocused probes are however incompatible with the conditions required for atomic resolution ADF-STEM imaging, and so cannot be used simultaneously with the incoherent Z-contrast imaging. A recent development combining a ptychography method called Wigner-distribution deconvolution (WDD) [16,24] and a fast pixelated detector shows that it not only allows simultaneous atomic resolution phase and ADF Z-contrast imaging, but also enables direct measurement and removal of residual lens aberrations through post-acquisition processing, and allows "optical-sectioning" to obtain three-dimensional information using only one experimental dataset under a fixed focusing condition [25].

Although ptychography 4D-STEM under zero defocus offers a phase image that can be combined with simultaneous Z-contrast imaging, its approximately sine-shaped contrast transfer function at low spatial frequencies [26] remains to be improved. Recently, it has been shown that introducing a phase plate at the probe forming aperture of a STEM, which is equivalent to a Zernike phase plate in the back focal plane of a TEM [27] based on the principle of reciprocity [28], leads to a phase contrast transfer function (PCTF) that depends on the cosine of the aberration wave shift [29]. Another study demonstrated that the introduction of a patterned pre-specimen phase plate in the probe forming aperture

combined with a virtual detector whose geometry matches that of the phase plate, a method called "matched illumination detector interferometry" (MIDI-STEM) [30], gives a linear phase image with enhanced contrast transfer of low spatial frequency specimen information. Similarly, the introduction of a phase plate in X-ray diffraction experiments has also been shown to improve the phase retrieval by enhancing the interferences between the diffracted waves collected in the far field [31].

Here we introduce a 4D-STEM phase contrast imaging method called ptychographic MIDI-STEM (PMIDI-STEM), to combine the advantage of a phase plate in enhancing the low frequency contrast transfer [30] and the advantage of ptychography 4D-STEM [13,26] in maximising the extraction of phase information and simultaneous formation of Z-contrast imaging. We perform theoretical calculations to compare the PCTF of PMIDI-STEM to that of MIDI-STEM, ptychography 4D-STEM at zero defocus as well as ptychography with a largely defocused probe. We show a proof-of-principle experimental result of imaging gold nanoparticles on an ultra-thin amorphous carbon substrate, and perform multislice image simulations of a heterogeneous DNA bio-molecule attached to Au nanoparticles under low dose imaging conditions to demonstrate the potential applications of imaging weakly scattering and beam sensitive materials at low dose.

2. Experimental setup

Fig. 1a shows an averaged convergent beam electron diffraction (CBED) pattern of an ultra-thin carbon sample, using a STEM probe formed by inserting a MIDI-STEM phase plate into the probe forming aperture plane. The MIDI-STEM phase plate is an equal-area *Fresnel* zone plate with 20-ring pairs, fabricated using FIB milling of a SiN membrane [32]. With such a geometry, the electron probe shows an atomically sharp central peak with enhanced probe tails as shown in 1b, which enables incoherent Z-contrast imaging to be simultaneously combined with the phase imaging at atomic resolution. The enhanced intensities at the probe tail improves the amount of overlap in illuminated areas, which helps to improve the PCTF of low frequencies.

The 4D-STEM data consisting of a transmitted electron diffraction pattern at each probe position was recorded using a Gatan K2 IS direct electron detector with 3840×3712 pixels, operated at 400 frames per second and binned by 2. The camera acquisition

and probe scanning were synchronized using a Gatan Digiscan. For the experimental data demonstrated in this work, the electron probe was scanned over a 14.5 nm field-of-view with 256×256 probe positions to create a $256 \times 256 \times 1920 \times 1792$ 4D-STEM data set consisting of 420 GB of raw images.

3. Ptychography reconstruction method

3.1. Phase retrieval with ptychography

Fig. 2 shows a schematic illustration of the ptychography re-construction procedure used to retrieve the phase from the re-corded 4D dataset. The method demonstrated here is a Fourier based non-iterative phase retrieval method extended from the previous work [13,17], and modified to accommodate the presence of a phase plate in the probe-forming aperture. The recorded 4D data consisting of a convergent beam electron diffraction (CBED) pattern at every probe position $\mathbf{r_p}$ is Fourier transformed with respect to probe positions $\mathbf{r_p}$, which transforms the 4D data into a doubly-reciprocal space complex 4D matrix $G(\mathbf{K_f}, \mathbf{Q_p})$, with two dimensions being the scattering vector $\mathbf{K_f}$ in the diffraction plane and the other two dimensions being the reciprocal space vector $\mathbf{Q_p}$ of the real space probe positions [13,17]. The Fourier transform with respect to probe positions interferes the electron wave at every probe position with those at its neighboring positions in a similar way to off-axis holography [33], but instead of using a physical biprism to generate a reference wave in holography, the electron waves at neighboring probe positions serve as the re-ference beam.

Under the weak phase object approximation (WPOA), $G(\mathbf{K_f}, \mathbf{Q_p})$ can be approximated as a linear function of the interferences be-tween the direct electron beam and two first order diffracted beams $\pm\mathbf{Q_p}$:

$$G(\mathbf{K_f}, \mathbf{Q_p}) = |A(\mathbf{K_f})|^2\delta(\mathbf{Q_p}) + A(\mathbf{K_f})A^*(\mathbf{K_f} + \mathbf{Q_p})\Psi^*(-\mathbf{Q_p}) + A^*(\mathbf{K_f})$$
$$A(\mathbf{K_f} - \mathbf{Q_p})\Psi(+\mathbf{Q_p}), \tag{1}$$

where $\mathbf{K_f}$ is the scattering vector and $\mathbf{Q_p}$ is the reciprocal vector of the real space probe position $\mathbf{r_p}$. $A(\mathbf{K_f})$ is the probe forming aperture function and $\Psi(\mathbf{Q_p})$ is the Fourier transform of the object transmission function as a function of spatial frequency $\mathbf{Q_p}$ and would be the scattered wave function under conditions of plane-wave illumination. Under the weak phase approximation, it has been proven [17] that the object transmission function satisfies the following:

$$\Psi(\mathbf{Q_p}) = -\Psi^*(-\mathbf{Q_p}). \tag{2}$$

Therefore, Eq. (1) can be simplified as:

$$G(\mathbf{K_f}, \mathbf{Q_p}) = |A(\mathbf{K_f})|^2\delta(\mathbf{Q_p}) + \Gamma_A(\mathbf{K_f}, \mathbf{Q_p})\Psi(\mathbf{Q_p}), \tag{3}$$

where the term $\Gamma_A(\mathbf{K_f}, \mathbf{Q_p})$ in Eq. (3) is a spatial frequency $\mathbf{Q_p}$ dependant aperture-overlap function that describes the inter-ference between the first order diffracted beams and the direct electron beam:

$$\Gamma_A(\mathbf{K_f}, \mathbf{Q_p}) = A^*(\mathbf{K_f})A(\mathbf{K_f} - \mathbf{Q_p}) - A(\mathbf{K_f})A^*(\mathbf{K_f} + \mathbf{Q_p}). \tag{4}$$

Based on Eq. (3), the 4D dataset $G(\mathbf{K_f}, \mathbf{Q_p})$ can be expressed as a set of linear terms of $\Gamma_A(\mathbf{K_f}, \mathbf{Q_p})\Psi(\mathbf{Q_p})$ for a set of experimental values of spatial frequency $\mathbf{Q_p}$ and detector pixel $A(\mathbf{K_f})$. Assuming the probe-forming aperture function $A(\mathbf{K_f})$ is known, the aperture-overlap function $\Gamma_A(\mathbf{K_f}, \mathbf{Q_p})$ can be calculated and therefore the object transmission function $\Psi(\mathbf{Q_p})$ can be solved at every spatial frequency $\mathbf{Q_p}$ from Eq. (3) directly [13,17].

Under zero lens aberrations and without a phase plate, $A(\mathbf{K_f})$ is a top hat function. With the presence of a MIDI-STEM phase plate [30] at the probe-forming aperture plane (see Fig. 1) $A(\mathbf{K_f})$ can be described as:

$$A(\mathbf{K_f}) = \begin{cases} 1, & \text{for } \mathbf{K_f} \in \text{Zone 1} \\ +i, & \text{for } \mathbf{K_f} \in \text{Zone 2}, \end{cases} \tag{5}$$

where Zone 1 and Zone 2 are regions of the phase plate with different thicknesses to produce zero (black rings) and $\pi/2$ (white rings) phase shift, respectively. It has been shown in the previous work (supplementary information of [30]) that the geometry of the phase plate is unimportant as long as it is known. For example, the phase plate can consist of randomly distributed Zone 1 and Zone 2 regions of equal total area. In this work, we use a geometry
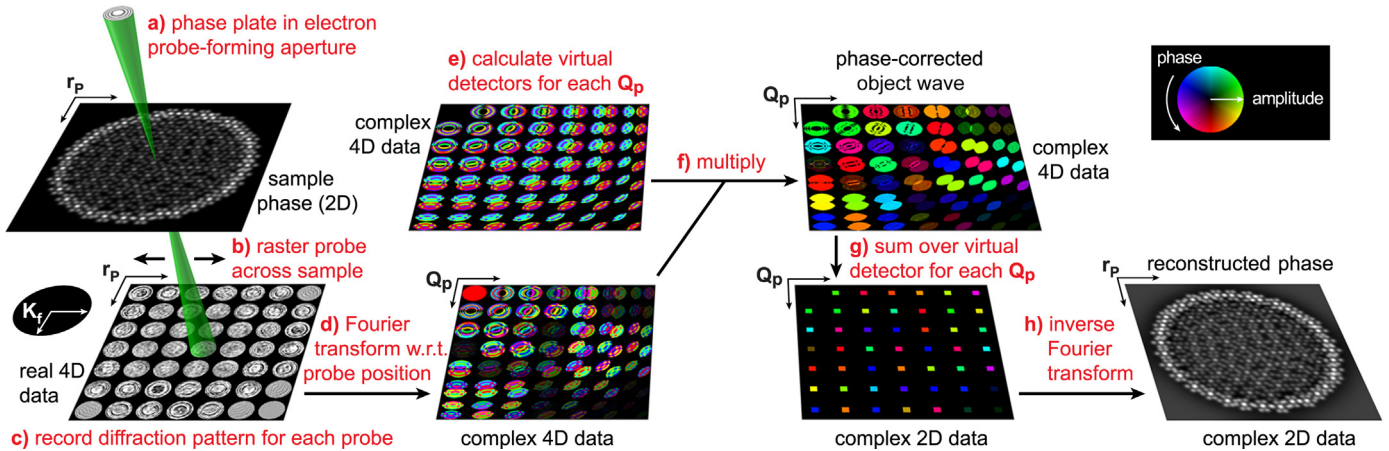

Fig. 2. Schematics of the PMIDI-STEM setup and the ptychographic reconstruction procedure. (a) A phase plate is used in the probe forming aperture, and (b) a fast pixelated detector collects the diffraction patterns synchronously with the STEM probe raster-scan, forming a real 4D data cube (c). (d) The real 4D data is Fourier transformed with respect to probe positions $\mathbf{r_p}$, resulting in a complex 4D data in the frequency domain ($\mathbf{Q_p}$) of the real space probe positions. The complex 4D data is a consequence of every diffracted electron wave interfering with its neighboring waves, and visually appear as the probe-forming apertures overlapped with a pair of apertures being shifted by $\pm\mathbf{Q_p}$. (e) A set of frequency ($\mathbf{Q_p}$) dependant complex virtual detectors consisting of overlapping apertures can be synthesized based on the geometry and the phase shift from the phase plate. (f) These virtual detectors can be used to remove the phase plate induced phase variation inside the aperture-overlap interference patterns, leading to a phase-corrected object wave at each frequency $\mathbf{Q_p}$. (g) After phase correction, the object function in the frequency domain ($\mathbf{Q_p}$) can be calculated by integrating the complex object wave over the detector plane $\mathbf{K_f}$. (h) Inverse Fourier transform of the object function with respect to $\mathbf{Q_p}$ leads to the final reconstructed complex object function in real space $\mathbf{r_p}$.

No phase plate

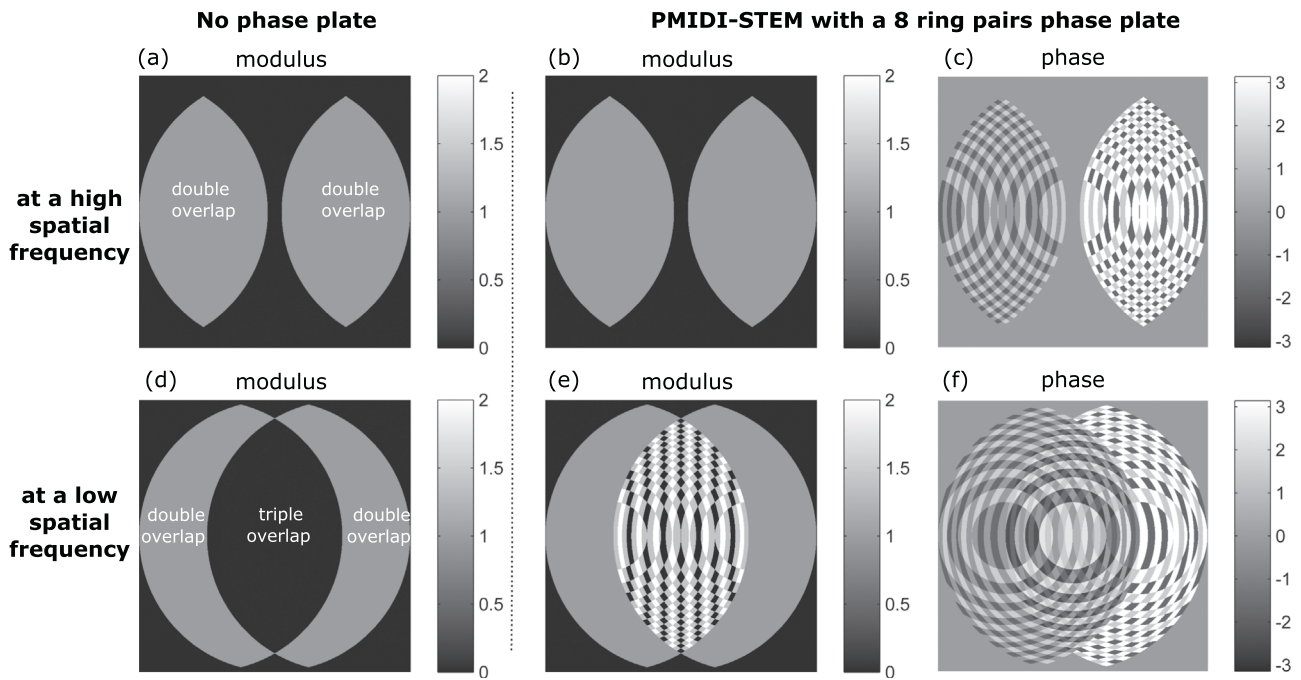**PMIDI-STEM with a 8 ring pairs phase plate**

Fig. 3. Schematic illustration of electron interferences inside the aperture-overlap formed by two first order diffracted beams and the direct beam described by $\Gamma_A(\mathbf{K_f}, \mathbf{Q_p})$. The interferences between the direct beam with the two diffracted beams form two double-overlap regions at high spatial frequencies, with an example shown in a, b, c; all three beams interfere to form a triple-overlap region at low spatial frequencies, with an example shown in d, e, f. In the case of zero aberrations without a phase plate in a, d, the phase in the triple-overlap region is completely cancelled showing zero modulus. With the presence of a phase plate in b, c, e, f, the phase inside the triple-overlap regions is not cancelled, instead shows a strong modulus.
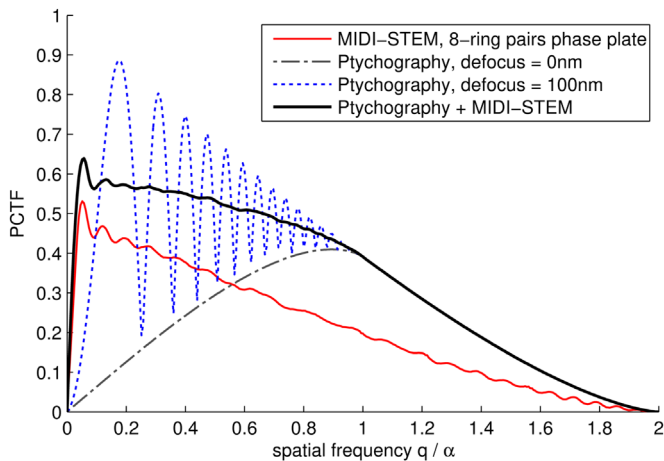

Fig. 4. PCTF of ptychography MIDI-STEM (PMIDI-STEM) with a 8-ring pairs phase plate. For comparison, the PCTF of MIDI-STEM with the same phase plate (red solid line), ptychography 4D-STEM at zero defocus (dash-dot line), as well as ptychography 4D-STEM with a 100 nm defocused probe (dotted line) are shown for comparison. The maximum spatial frequency being transferred is twice the convergence semi-angle of the probe forming aperture α, corresponding to a theoretical resolution limit of 0.058 nm for 300 keV beam energy and 17 mrad convergence semi-angle.

of circular ring pairs in order to ensure an azimuthal uniform phase contrast transfer.

A schematic illustration of the modulus and phase in the aperture-overlap areas described by $\Gamma_A(\mathbf{K_f}, \mathbf{Q_p})$ is shown in Fig. 3. The modulus of $\Gamma_A(\mathbf{K_f}, \mathbf{Q_p})$ represents the strength of contrast transfer of phase information through beam interferences. As shown in Fig. 3, the two diffracted beams overlap with the direct beam to form two "double-overlap" regions on the detector at high spatial frequencies $\mathbf{Q_p} > \alpha$ (where α is the probe forming convergence semi-angle) in Fig. 3a–c, and all three beams overlap to form two "double-overlap" regions and a "triple-overlap" region at

low spatial frequencies $\mathbf{Q_p} \leq \alpha$ in Fig. 3d–e. As shown previously [13,26], in the case of zero lens aberrations without a phase plate, phase information is transferred only through the double-overlap regions at all spatial frequencies, and no phase information is transferred through the triple-overlap region (Fig. 3d) because the two diffracted beams are anti-phase and leads to descructive interference with zero modulus under zero defocus aberration. This changes when a large defocus aberration (for example a 100 nm defocus) is injected into the probe-forming aperture, resulting in a strong phase ramp inside the disc-overlap regions and therefore stronger interferences (both constructive and destructive interferences) inside the triple overlap region. Similar to the effect of a large defocus, a *Fresnel* phase plate introduces $\pi/2$ phase shift inside the probe-forming aperture, and leads to strong interferes in the triple-overlap region shown in Fig. 3e. In summary, the beam interferences described by $\Gamma_A(\mathbf{K_f}, \mathbf{Q_p})$ suggest that both defocus aberrations and the presence of a phase plate can improve the contrast transfer of low frequency phase information through the triple-overlap region by introducing additional phase shift inside the aperture function.

To extract the maximum phase information recorded in the 4D data, we use ptychography to make use of the phase information at every detector pixel $\mathbf{K_f}$ for each spatial frequency $\mathbf{Q_p}$. In the case of zero aberrations and no phase plate in the probe-forming aperture, the ptychographic reconstruction is straightforward because every detector pixel $\mathbf{K_f}$ inside a disc-overlap region has the same phase value, and the object function at every spatial frequency $\mathbf{Q_p}$ can be reconstructed by integrating the complex value at each detector pixel $\mathbf{K_f}$ inside one side of the double-overlap regions, as demonstrated previously [13,26]. The introduction of a large defocus aberration or a MIDI phase plate with a $\pi/2$ phase shift (in Fig. 3) leads to phase variations inside the aperture-overlap region. Such phase variations restrict the use of the simple integration approach, which will result in phase cancellation and a loss of phase information in the final reconstruction. Based on the
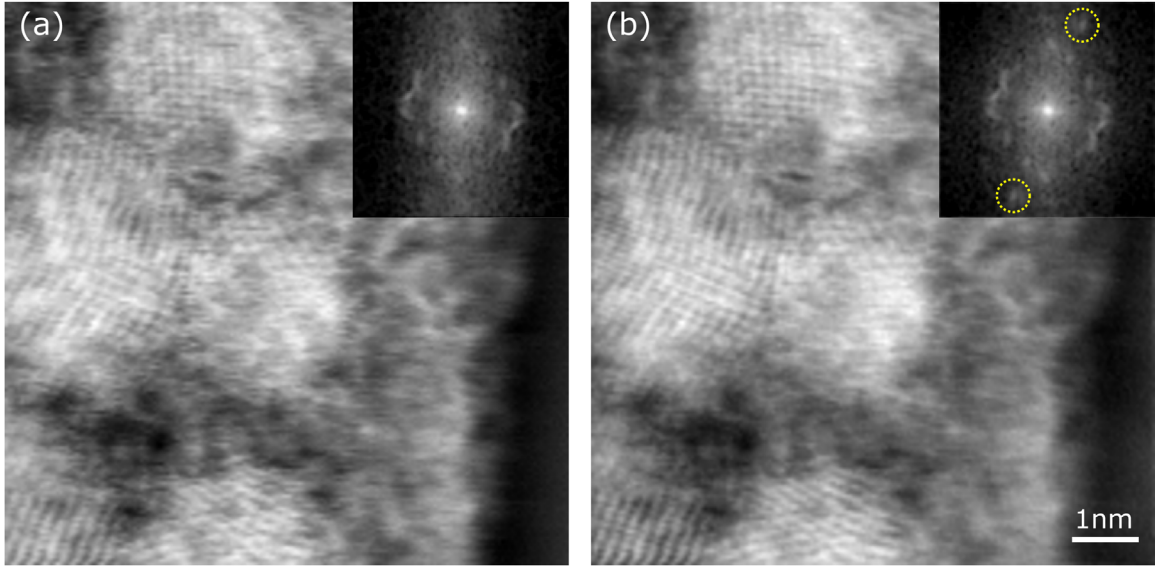
Fig. 5. Experimental phase images of Au on an ultra-thin carbon support using (a) MIDI-STEM and (b) PMIDI-STEM combining ptychography with a 20-ring pairs phase plate. The inset shows a diffractogram of the top left part of the image consisting of 3 nanoparticles, and the dashed circles indicate diffraction spots that are much stronger using PMIDI-STEM than using MIDI-STEM.

weak phase object approximation, such phase variations due to lens aberrations or a phase plate can be compensated using a complex "virtual detector" (see Fig. 2) for each spatial frequency $\mathbf{Q_p}$, which serves to correct the phase variations inside the disc-overlap regions so that the phases at all detector pixels $\mathbf{K_f}$ can be integrated constructively afterwards. The virtual detector is defined as the normalized complex conjugate of the aperture-overlap function $\Gamma_A(\mathbf{K_f}, \mathbf{Q_p})$, and it compensates the phase variations inside the aperture-overlap by a simple multiplication operation given in Eq. (6). After the phase-compensation is performed, the object function can be obtained using the same phase integration procedure as for zero aberration case [13,26] following Eq. (6), with the only difference being that the phase inside triple-overlap regions is now included in this method. Inverse Fourier transform of $\Psi(\mathbf{Q_p})$ with respect to the spatial frequency $\mathbf{Q_p}$ leads to the final reconstructed complex object transmission function in real space.

$$\Psi(\mathbf{Q_p}) = \sum_{\mathbf{K_f}} \left\{ G(\mathbf{K_f}, \mathbf{Q_p}) \cdot \frac{\Gamma_A^*(\mathbf{K_f}, \mathbf{Q_p})}{|\Gamma_A(\mathbf{K_f}, \mathbf{Q_p})|} \right\}, \quad \text{for } \mathbf{K_f} \in \{ |\Gamma_A(\mathbf{K_f}, \mathbf{Q_p}) | \neq 0 \}. \tag{6}$$

Correcting the phase shift from the phase plate using a virtual detector in Fig. 2 allows the phase at all detector pixels $\mathbf{K_f}$ to be integrated constructively to give the best phase contrast. The virtual detector also imposes an inherent filter of the noise outside the aperture-overlap region without reducing the strength of the phase signal. Though the virtual detector requires explicit knowledge about the phase plate in the probe-forming aperture, the physical geometry of the phase plate is experimentally straightforward to measure, as shown in Fig. 1, and the thickness of the SiN membrane can be controlled using FIB milling to give the expected $\pi/2$ phase shift [32]. An independent measurement of the phase inside the probe-forming aperture can also be obtained using the iterative ptychography methods [19,21] or ptychography Wigner-distribution deconvolution approach [25], which will be explored in future work.

3.2. PCTF calculations

As discussed above, Eq. (3) indicates that the phase information of the object $\Psi(\mathbf{Q_p})$ is transferred through the beam interfering aperture-overlap region described by $\Gamma_A(\mathbf{K_f}, \mathbf{Q_p})$. The modulus of the aperture-overlap function describes the strength of the phase information present inside the aperture-overlap regions, and thus provides a quantitative measurement of PCTF. The PCTF of ptychography can be calculated as the total area of aperture-overlap regions which carry phase information (i.e., with non-zero $|\Gamma_A(\mathbf{K_f}, \mathbf{Q_p})|$), normalized by the total area of the bright field disc as following:

$$\text{Ptychography: PCTF}(\mathbf{Q_p}) = \frac{1}{2} \frac{\sum_{\mathbf{K_f}} |\Gamma_A(\mathbf{K_f}, \mathbf{Q_p})|}{\sum_{\mathbf{K_f}} |A(\mathbf{K_f})|} \tag{7}$$

Eq. (7) gives the PCTF of ptychography that is applicable to all three cases under investigation in this work, including ptychography 4D-STEM under zero aberration condition without a phase plate, ptychography 4D-STEM using a largely defocused probe, and ptychography MIDI-STEM. Note that under WPOA and zero aberration condition used in Eqs. (2) and (3), the object phase can be determined using either $+\mathbf{Q_p}$ or $-\mathbf{Q_p}$ side of the overlapping discs, therefore a pre-factor of 1/2 is used in Eq. (7) for the PCTF calculations. This pre-factor in Eq. (7) leads to a PCTF value that is half of the PCTF defined in the previous work [26].

The PCTF of ptychography is also compared to that of MIDI-STEM in a previous work [30], in which the phase image is synthesized at every probe position by integrating the diffraction intensity over a simple virtual detector MIDI($\mathbf{K_f}$) described in Eq. (8). The diffraction signal being integrated over the detector predominantly results from the dot product of the imaginary part of $\Gamma_A(\mathbf{K_f}, \mathbf{Q_p})$ and the phase of the object, in the same way as a HRTEM phase plate which uses a $\pi/2$ phase shift to convert the object phase to directly measurable diffraction intensities [34]. Therefore the corresponding PCTF can be mathematically described as:

$$\text{MIDI}(\mathbf{K_f}) = \begin{cases} +1, & \text{for } \mathbf{K_f} \in \text{Zone 1} \\ -1, & \text{for } \mathbf{K_f} \in \text{Zone 2} \end{cases} \tag{8}$$

$$\text{MIDI: PCTF}(\mathbf{Q_p}) = \frac{\text{Im}\{ \sum_{\mathbf{K_f}} (\Gamma_A(\mathbf{K_f}, \mathbf{Q_p}) \cdot \text{MIDI}(\mathbf{K_f})) \}}{2 \sum_{\mathbf{K_f}} |A(\mathbf{K_f})|} \tag{9}$$

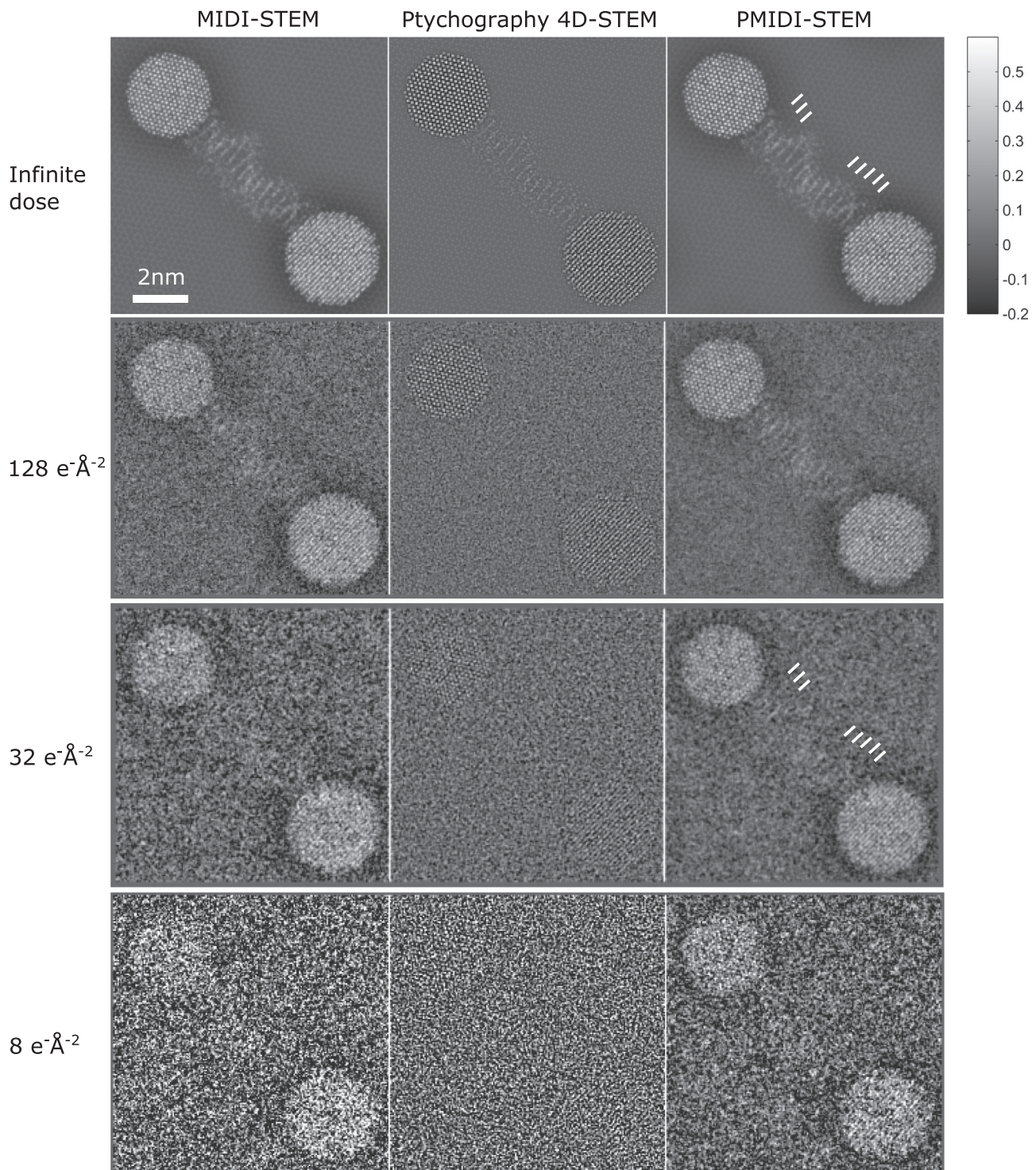Fig. 4 shows the PCTF of PMIDI-STEM with 8-ring pairs,

Fig. 6. Multislice simulations of phase contrast imaging of a DNA snippet connecting two gold nanoparticles on a single layer of graphene substrate. The phase images were reconstructed using PMIDI-STEM, MIDI-STEM, as well as ptychography 4D-STEM without a phase plate under zero lens aberration. Several electron doses are simulated for comparison. The white lines indicate some of the DNA strands that are visible under the dose of $32\,e^-\text{Å}^{-2}$. The phases obtained from the ptychography methods are quantitative with a scale bar in unit of radian.

compared to that of MIDI-STEM and ptychography 4D-STEM without phase plate under both zero aberration and 100 nm-defocus aberration. It can be seen that in the relatively high spatial frequency range (where the scattering vector q is larger than the convergence angle α), ptychography improves the PCTF by approximately a factor of two compared to MIDI-STEM. In the relatively low spatial frequency range ($0 < q \leq \alpha$), MIDI-STEM gives a better PCTF than ptychography 4D-STEM under the zero defocus

condition, as explained above in terms of the difference in contrast transfer through the triple-overlap region in Fig. 3d and e. Ptychography with a large defocus aberration also shows an enhanced contrast transfer at low frequencies, as shown from the dotted line in Fig. 4. Although a largely defocused probe has been widely adopted by various iterative ptychography methods in literature [19,21], Fig. 4 shows that the PCTF varies strongly with spatial frequencies, because the large phase ramp inside the disc-
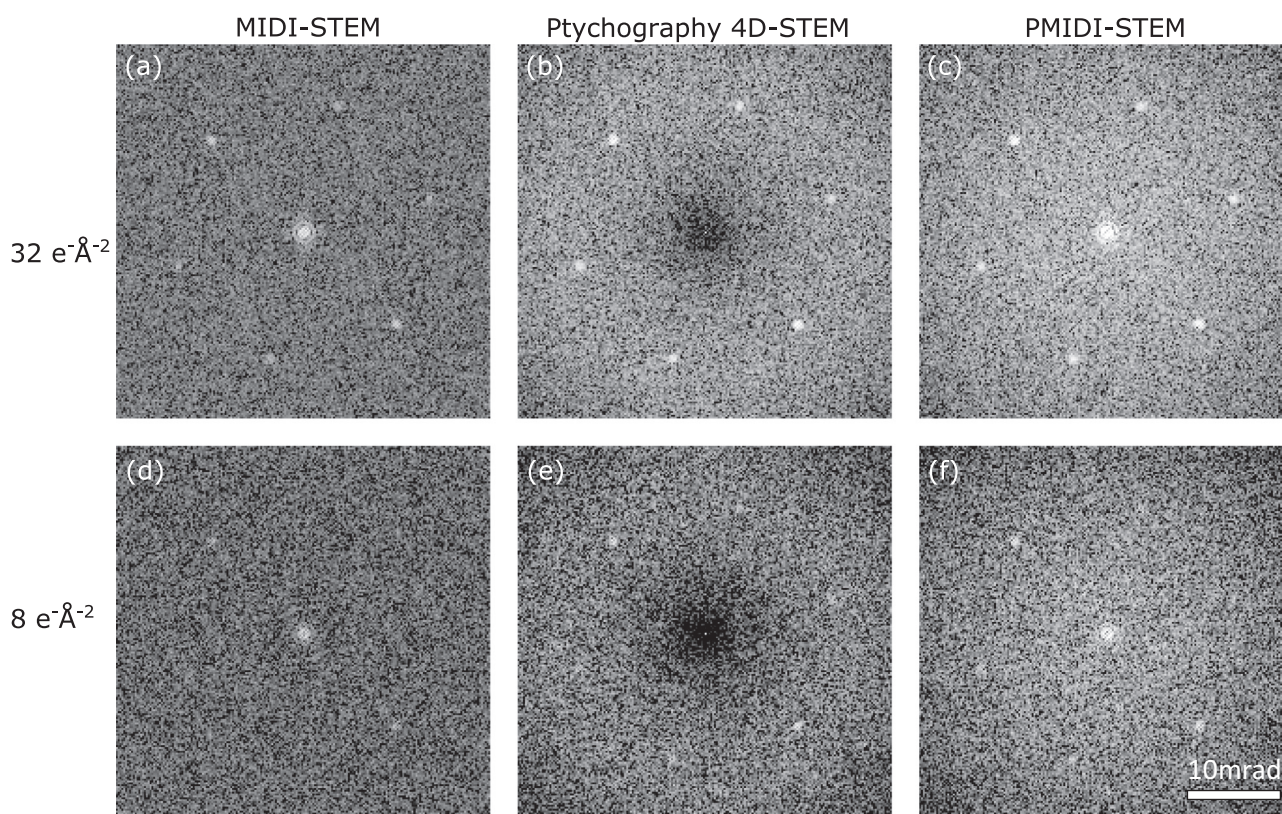
MIDI-STEM   Ptychography 4D-STEM   PMIDI-STEM

Fig. 7. Diffractograms obtained from the Fourier transform of the phase images to compare the visibility of Au atomic lattices of different methods under the electron dose of 32 and $8e^-Å^{-2}$. The ptychography 4D-STEM phase image is obtained under the zero aberration condition. The intensities of the FT images are in log scale and adjusted to have roughly the same contrast of background.
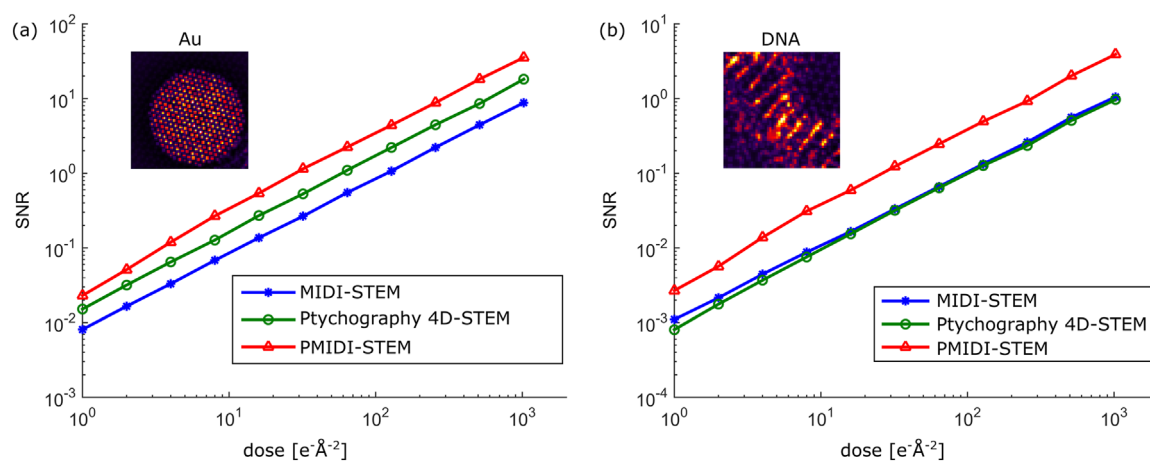

Fig. 8. Comparison of phase image SNR as a function of the electron dose for the three phase retrieval methods. Two image sub-regions consisting of the Au nanoparticle and the DNA structure are used to evaluate the SNR performance of strongly-scattering and weakly-scattering objects, respectively. The ptychography 4D-STEM phase image is obtained under the zero aberration condition.

overlap region as a result of the large defocus aberration also has a strong dependence on spatial frequencies $\mathbf{Q_p}$. In comparison, using a phase plate, the PMIDI-STEM method gives a much smoother and overall rather efficient PCTF under zero defocus aberration, which is the optimal condition for simultaneous Z-contrast or spectroscopy imaging in STEM.

4. Results and discussion

A proof of principle study was performed using a sample of Au nanoparticles on a carbon support and shown in Fig. 5. For a direct comparison, both MIDI-STEM Fig. 5a and PMIDI-STEM Fig. 5b have been applied to retrieve the phase from the same 4D data. Both phase images give a high visibility of the ultra-thin carbon support as well as the Au nanoparticles demonstrating both methods provide a high sensitivity in imaging light elements. And because of the improved PCTF of PMIDI-STEM compared to MIDI-STEM especially in the higher spatial frequency range, the contrast of high frequency phase information is improved. Clearly shown in Fig. 5, the high order Fourier spots of the Au lattice are much stronger in the diffractograms of PMIDI-STEM than in MIDI-STEM, as indicated by circles in Fig. 5.

To explore the potential limits of this phase contrast method

especially in imaging beam sensitive biological structures, we performed a multislice simulation of a DNA snippet connecting two gold nanoparticles on a single layer of graphene, as shown Fig. 6. The same simulation model as in the previous work [30] is used for consistent comparisons. Multislice image simulations were performed using custom MATLAB codes that follow the methods of Kirkland [2], using the same experiment conditions as in the experiment shown in Fig. 5 and 8 frozen-phonon configurations. Electron doses of infinity, 128, 32 and 8 $e^-\mathring{A}^{-2}$ were used to simulate the CBED patterns in the 4D data. The noise in the simulations includes only the Poisson distributed shot noise and no detector readout noise.

As shown in Fig. 6, the PMIDI-STEM method in this work clearly gives the best phase image of both the DNA structure and the Au nanoparticles, as compared to MIDI-STEM and the ptychography 4D-STEM method without a phase plate. Using PMIDI-STEM, the atomic details of both the double-helix and the DNA strands are clearly visible under the dose of $128\ e^-\mathring{A}^{-2}$. The signal strength remains high enough to show a higher than background image contrast of the DNA, with some of the DNA strands being visible under an electron dose of $32\ e^-\mathring{A}^{-2}$. The improved low dose performance of PMIDI-STEM compared to MIDI-STEM is attributed to two reasons, first of all an improved PCTF over the entire spatial frequency range, and secondly the ability of ptychography to reject noise outside the disc-overlap regions which is otherwise included by the MIDI-STEM virtual detector into the final image.

Thanks to the enhanced PCTF of low spatial frequencies in MIDI-STEM and PMIDI-STEM, the shape and location of the Au nanoparticles, which are primarily low frequency information, improves the visibility of the nanoparticles at an extremely low dose of $8\ e^-\mathring{A}^{-2}$. As shown in Fig. 6, the visibility of Au nanoparticles are much better using PMIDI-STEM than using ptychography 4D-STEM. As for high frequency information, we compared the diffractogram of the simulated low dose Au-DNA snippet images in Fig. 7. Consistent with the PCTF calculations in Fig. 4, both PMIDI-STEM and ptychography 4D-STEM show stronger diffraction spots of Au lattice than MIDI-STEM, and the atomic resolution information survives at such an extremely low dose of $8\ e^-\mathring{A}^{-2}$ using ptychography. In summary, a highly efficient PCTF at both low and high frequencies offered by PMIDI-STEM can be beneficial for imaging not only DNA but also Au nanoparticles, with the low spatial frequency transfer being useful for identifying the shape and thickness profile of the nanoparticle, and high frequency transfer for revealing its atomic resolution structure details.

Fig. 8 shows the SNR as a function of electron dose using the dose series multislice simulations of the Au/DNA structure. To evaluate the SNR of both strongly and weakly scattering objects, the SNR plots are calculated from two image regions consisting of only Au and DNA, respectively. Compared to MIDI-STEM, PMIDI-STEM shows approximately a factor of two improvement in SNR for imaging both Au lattice and DNA. The SNR of ptychography 4D-STEM is better than that of MIDI-STEM for imaging Au atomic lattices, which is consistent with the PCTF calculations of a better high frequency contrast transfer using ptychography 4D-STEM than using MIDI-STEM.

5. Conclusion

In this work we demonstrate a new STEM phase imaging method, PMIDI-STEM, which combines a phase plate in the probe-forming aperture, a fast pixelated detector to record the 4D-STEM data, and a ptychography phase reconstruction method to maximize the extraction of phase information. Theoretical calculations suggest that PMIDI-STEM gives a close to linear PCTF that is

efficient in both low and high spatial frequencies. A proof of principle experiment demonstrates that PMIDI-STEM is sensitive to both light and heavy elements, and the improved PCTF leads to more phase information being transferred compared to MIDI-STEM. Multislice low dose image simulations on a Au-DNA snippet sample suggests it's promising to image soft matter at nearly atomic resolution with a close to "critical dose" of less than $50\ e^-\mathring{A}^{-2}$. The low dose performance provides a potential opportunity for imaging a wide range of beam sensitive materials and biological structures. The sensitivity to both lightly and heavily scattering objects at low and high spatial frequencies is particularly interesting in imaging hetero-structures composed of both hard and soft matter especially at their interfaces. The close to linear PCTF offers a directly interpretable phase image without comparing to image simulations, and the phase image can be obtained at zero defocus, which is highly advantageous compared to the large defocus values required for phase contrast imaging in CTEM. The fact that the STEM probe retains its atomic resolution with the presence of the phase plate also allows simultaneous atomic resolution incoherent ADF imaging to be combined with the phase image, which can be very beneficial compared to ptychography methods using heavily defocused electron probe.

Acknowledgements

References

[1] R. Henderson, The potential and limitations of neutrons, electrons and x-rays for atomic resolution microscopy of unstained biological molecules, Q. Rev. Biophys. 28 (02) (1995) 171–193.
[2] E. Kirkland, Advanced Computing in Electron Microscopy, Springer Science & Business Media, New York, 2010.
[3] K. Downing, R. Glaeser, Restoration of weak phase-contrast images recorded with a high degree of defocus: the twin image problem associated with CTF correction, Ultramicroscopy 108 (9) (2008) 921–928.
[4] R. Danev, B. Buijsse, M. Khoshouei, J. Plitzko, W. Baumeister, Volta potential phase plate for in-focus phase contrast transmission electron microscopy, Proc. Nat. Acad. Sci. 111 (44) (2014) 15635–15640.
[5] E. Majorovits, B. Barton, K. Schultheiss, F. Perez-Willard, D. Gerthsen, R. Schröder, Optimizing phase contrast in transmission electron microscopy with an electrostatic (boersch) phase plate, Ultramicroscopy 107 (2) (2007) 213–226.
[6] H. Rose, Phase contrast in scanning transmission electron microscopy, Optik 39 (4) (1974) 416–436.
[7] S. Findlay, N. Shibata, H. Sawada, E. Okunishi, Y. Kondo, Y. Ikuhara, Dynamics of annular bright field imaging in scanning transmission electron microscopy, Ultramicroscopy 110 (7) (2010) 903–923.
[8] N. Dekkers, H. De Lang, Differential phase contrast in a STEM, Optik 41 (4) (1974) 452–456.
[9] H. Rose, Nonstandard imaging methods in electron microscopy, Ultramicroscopy 2 (1977) 251–267.
[10] N. Shibata, S. Findlay, Y. Kohno, H. Sawada, Y. Kondo, Y. Ikuhara, Differential phase-contrast microscopy at atomic resolution, Nat. Phys. 8 (8) (2012) 611–615.
[11] K. Müller, F. Krause, A. Béché, M. Schowalter, V. Galioit, S. Löffler, J. Verbeeck, J. Zweck, P. Schattschneider, A. Rosenauer, Atomic electric fields revealed by a quantum mechanical approach to electron picodiffraction, Nat. Commun. 5 (2014) 5653.
[12] E. Waddell, J. Chapman, Linear imaging of strong phase objects using asymmetrical detectors in STEM, Optik 54 (2) (1979) 83–96.
[13] T. Pennycook, A. Lupini, H. Yang, M. Murfitt, L. Jones, P. Nellist, Efficient phase contrast imaging in STEM using a pixelated detector part 1: experimental demonstration at atomic resolution, Ultramicroscopy 151 (2015) 160–167.
[14] H. Yang, L. Jones, H. Ryll, M. Simson, H. Soltau, Y. Kondo, R. Sagawa, H. Banba,

I. MacLaren, P. Nellist, 4D STEM: High efficiency phase contrast imaging using a fast pixelated detector, J. Phys. Conf. Ser. 644 (2015) 012032.

[15] W. Hoppe, Beugung im inhomogenen primärstrahlwellenfeld i. prinzip einer phasenmessung von elektronenbeugungsinterferenzen, Acta Crystallogr. Sect. A: Cryst. Phys. Diffr. Theor. Gen. Crystallogr. 25 (4) (1969) 495–501.

[16] J. Rodenburg, R. Bates, The theory of super-resolution electron microscopy via wigner-distribution deconvolution, Philos. Trans. R. Soc. Lond. A: Math. Phys. Eng. Sci. 339 (1655) (1992) 521–553.

[17] J. Rodenburg, B. McCallum, P. Nellist, Experimental tests on double-resolution coherent imaging via STEM, Ultramicroscopy 48 (3) (1993) 304–314.

[18] J. Rodenburg, A. Hurst, A. Cullis, B. Dobson, F. Pfeiffer, O. Bunk, C. David, K. Jefimovs, I. Johnson, Hard-x-ray lensless imaging of extended objects, Phys. Rev. Lett. 98 (3) (2007) 034801.

[19] P. Thibault, M. Dierolf, A. Menzel, O. Bunk, C. David, F. Pfeiffer, High-resolution scanning x-ray diffraction microscopy, Science 321 (5887) (2008) 379–382.

[20] P. Nellist, B. McCallum, J. Rodenburg, Resolution beyond the 'information limit' in transmission electron microscopy, Nature 374 (6523) (1995) 630–632.

[21] A. Maiden, J. Rodenburg, An improved ptychographical phase retrieval algorithm for diffractive imaging, Ultramicroscopy 109 (10) (2009) 1256–1262.

[22] M. Humphry, B. Kraus, A. Hurst, A. Maiden, J. Rodenburg, Ptychographic electron microscopy using high-angle dark-field scattering for sub-nanometre resolution imaging, Nat. Commun. 3 (2012) 730.

[23] A. D'Alfonso, A. Morgan, A. Yan, P. Wang, H. Sawada, A. Kirkland, L. Allen, Deterministic electron ptychography at atomic resolution, Phys. Rev. B 89 (6) (2014) 064101.

[24] H.N. Chapman, Phase-retrieval x-ray microscopy by wigner-distribution deconvolution, Ultramicroscopy 66 (3) (1996) 153–172.

[25] H. Yang, R. Rutte, L. Jones, M. Simson, R. Sagawa, H. Ryll, M. Huth, T. Pennycook, M. Green, H. Soltau, Y. Kondo, B. Davis, P. Nellist, Simultaneous atomic-resolution electron ptychography and Z-contrast imaging of light and heavy elements in complex nanostructures, Nat. Commun. 7 (2016) 12532.

[26] H. Yang, T. Pennycook, P. Nellist, Efficient phase contrast imaging in stem using a pixelated detector. part ii: optimisation of imaging conditions, Ultramicroscopy 151 (2015) 232–239.

[27] R. Danev, H. Okawara, N. Usuda, K. Kametani, K. Nagayama, A novel phase-contrast transmission electron microscopy producing high-contrast topographic images of weak objects, J. Biol. Phys. 28 (4) (2002) 627–635.

[28] J. Cowley, Image contrast in a transmission scanning electron microscope, Appl. Phys. Lett. 15 (2) (1969) 58–59.

[29] H. Minoda, T. Tamai, H. Iijima, F. Hosokawa, Y. Kondo, Phase-contrast scanning transmission electron microscopy, Microscopy 64 (2015) 181–187.

[30] C. Ophus, J. Ciston, J. Pierce, T.R. Harvey, J. Chess, B.J. McMorran, C. Czarnik, H. Rose, P. Ercius, Efficient linear phase contrast in scanning transmission electron microscopy with matched illumination and detector interferometry, Nat. Commun. 7 (2016) 10719.

[31] I. Johnson, K. Jefimovs, O. Bunk, C. David, M. Dierolf, J. Gray, D. Renker, F. Pfeiffer, Coherent diffractive imaging using phase front modifications, Phys. Rev. Lett. 100 (15) (2008) 155503.

[32] T.R. Harvey, J.S. Pierce, A.K. Agrawal, P. Ercius, M. Linck, B.J. McMorran, Efficient diffractive phase optics for electrons, New J. Phys. 16 (9) (2014) 093039.

[33] H. Lichte, Electron image plane off-axis holography of atomic structures, Adv. Opt. Electron Microsc. 12 (1991) 25–91.

[34] R. Danev, K. Nagayama, Complex observation in electron microscopy: Iv. reconstruction of complex object wave from conventional and half plane phase plate image pair, J. Phys. Soc. Jpn. 73 (10) (2004) 2718–2724.